

# Homoclinic chaos in a laser containing a saturable absorber

M. Lefranc, D. Hennequin, and D. Dangoisse

*Laboratoire de Spectroscopie Hertzienne, Associé au Centre National de la Recherche Scientifique, Université des Sciences et Techniques de Lille-Flandres-Artois, F-59655 Villeneuve d'Ascq Cedex, France*

Received August 15, 1989; accepted October 11, 1990

Checks of homoclinic chaos made with nonlinear analysis techniques have been performed on the signals coming from a CO<sub>2</sub> laser containing CH<sub>3</sub>I as a saturable absorber. The one-dimensional return maps of the regimes appearing inside the alternating periodic chaotic sequence are typical of homoclinic chaos. Numerical simulations give results in good agreement with the experimental observations. In the case of a fast absorber, a homoclinic tangency to a cycle created in a subcritical Hopf bifurcation is seen to be responsible for the homoclinic behavior observed in the model.

## 1. INTRODUCTION

A laser containing a saturable absorber (LSA) was studied extensively in connection with the requirement for easy and efficient modulation of CO<sub>2</sub> laser radiation, and many molecules have been used as saturable absorbers for passive Q switching (PQS). In the PQS regime, the laser is spontaneously unstable, and its output intensity exhibits periodic pulses of various shapes. In the beginning of the 1970's this PQS regime received much attention as new absorbing molecules were searched for, but only a few publications were devoted to the mechanisms from which PQS originates. To our knowledge, the first model able to reproduce the PQS shapes was a four-level model for both the laser medium and the absorber.<sup>1-4</sup> In the beginning of the 1980's there was renewed interest in the LSA as the field of optical instability grew.<sup>5</sup> New shapes of PQS pulses were discovered,<sup>6-8</sup> and the dual four-level model was unable to reproduce them correctly.<sup>9</sup> A three-plus-two-level model was then introduced by Tachikawa *et al.* to reproduce the entire experimentally observed phenomenology.<sup>7,8,10</sup> This model was later completed by the addition of a rotational-level bath in the gain medium.<sup>11</sup> Recently, chaotic pulses were observed both experimentally<sup>12,13</sup> and theoretically.<sup>14</sup> The dynamics of this chaos has been interpreted through a topological analysis of the phase space associated with the signal.<sup>12,13,15</sup>

The PQS regime usually corresponds to the existence of two unstable fixed points: the  $I_0$  point has zero intensity and is a saddle point and the  $I_+$  point has a nonzero intensity and is a saddle focus. As a control parameter is varied, the  $I_+$  point loses its stability through a Hopf bifurcation, generating type II PQS, which destabilizes through period doubling.<sup>12,16</sup> Then alternating periodic and chaotic sequences appear,<sup>12</sup> similar to those encountered in the neighborhood of a homoclinic bifurcation,<sup>17,18</sup> when some conditions specified by Shil'nikov<sup>19</sup> are satisfied. However, the situation here is complicated by the presence of the second fixed point in the phase space and possibly by a perturbation that is due to noise.<sup>20</sup>

To our knowledge, no characterization of the chaotic behavior inside the alternating periodic-chaotic sequence other than in the preliminary results given by us<sup>21</sup> and in

a related paper by Papoff *et al.*<sup>22</sup> has been made. Similar characterizations have been made for a CO<sub>2</sub> laser with feedback<sup>23</sup> and in the Belousov-Zhabotinskii reaction.<sup>24</sup> In fact, although chaos has been observed in the LSA, there has been no demonstration that this was Shil'nikov chaos and two phenomena may, in some situations, inhibit this chaotic behavior: the noise<sup>20</sup> and a strong attraction of  $I_0$  along its stable manifold, which can destroy sensitivity to the initial conditions.<sup>13,15</sup>

Here we report on an analysis that uses methods inspired by the dynamical system theory [phase portraits, Poincaré maps, and one-dimensional (1-D) maps] of the erratic behavior inside the alternating chaotic-periodic sequence. We show that in the CO<sub>2</sub> + CH<sub>3</sub>I LSA, in spite of the presence of a second fixed point in the phase space, the dynamics qualitatively follows the Shil'nikov behavior. We also study the evolution of the chaos between two periodic regimes and show that the transition from periodic behavior to chaos follows two different routes: period doubling on the one hand and the Pomeau-Manneville (type I intermittency) route on the other.

This paper is organized as follows: in Section 2 an analysis of experimental data is presented, showing that the PQS regime possesses the properties of the Shil'nikov chaos. In Section 3 the stability of the fixed points of a standard model of the LSA is discussed. The numerical solutions of this system are analyzed in Section 4 by using the same techniques as in Section 2 together with Floquet's theory.

## 2. EXPERIMENTS

The experimental device has already been described elsewhere.<sup>3</sup> It is composed of a CO<sub>2</sub> + CH<sub>3</sub>I LSA, in which amplification is obtained in a mixture of CO<sub>2</sub>, N<sub>2</sub>, and He in the approximate proportions of 3:6.5:1 for a total pressure of 7.8 Torr; the absorber is CH<sub>3</sub>I at a pressure of ~30 mTorr. The laser is tuned on the 10(P)32 line, in quasi-resonance with at least three absorption lines of CH<sub>3</sub>I.<sup>25</sup> The general behavior exhibited by the LSA when the cavity detuning or the pump parameter is varied in this region of the parameter space<sup>12</sup> shows a cw regime followed by a periodic regime that becomes chaotic through

a period-doubling cascade; then periodic and chaotic sequences alternate, as chemical reactions have shown.<sup>26</sup> Beyond this sequence, the laser is off. In the particular conditions of the results discussed below, the control parameter is the cavity detuning, and the observed order of behavior is cw,  $T$ ,  $2T$ ,  $4T$ , chaos,  $P^{(3)}$ ,  $C^{(2)}$ ,  $P^{(2)}$ ,  $C^{(1)}$ ,  $P^{(1)}$ ,  $P^{(0)}$ , off. The notation used here was introduced in Ref. 15 and may be summarized as follows:

- (i) The  $T$  regime refers to type II PQS: the output of the LSA is a  $T$  periodic oscillation, emerging from the cw regime through a Hopf bifurcation. It evolves toward chaos through a period-doubling cascade (regimes  $2^n T$ ).
- (ii) The  $P^{(n)}$  regimes refer to type I PQS: the output of the LSA exhibits periodic pulses composed of a narrow

high peak followed by a series of  $n$  undulations at period  $T$ . It has been observed<sup>12</sup> that the pulses also undergo a series of period doublings culminating in an erratic regime called  $C^{(n)}$  when the output is located in parameter domains between the  $P^{(n)}$  and  $P^{(n+1)}$  regions.

We have analyzed the erratic regimes  $C^{(n)}$  to find characteristic properties that support the existence of homoclinic chaos. The most remarkable one concerns the 1-D maps constructed from the Poincaré section of the attractor: the 1-D map of homoclinic chaos shows  $n + 1$  branches and possibly a part of an  $(n + 2)$ th one; each branch is associated with  $p$  spirals in the phase space ( $p \leq n$  or  $p \leq n + 1$ ), and the distance between the branches decreases when  $p$  increases. The number of

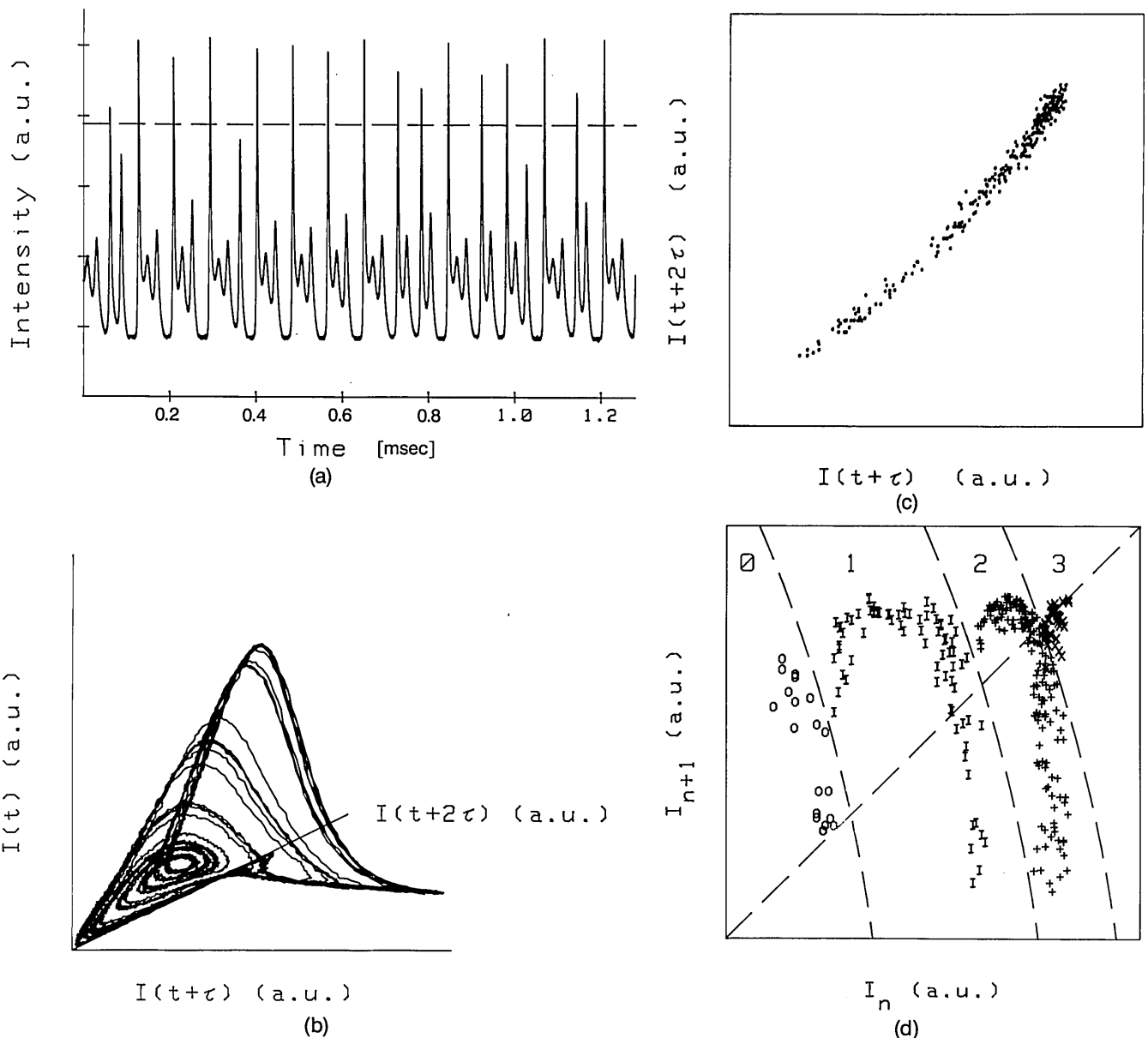


Fig. 1. Analysis of the  $C^{(2)}$  experimental regime: (a) temporal sequence; (b) three-dimensional reconstruction of the attractor in the phase space  $I(t)$ ,  $I(t + \tau)$ ,  $I(t + 2\tau)$ , where  $\tau = 3.2 \mu\text{sec}$ ; (c) Poincaré section performed in the reinjection loop of the attractor in a plane indicated by the dashed line in (a); (d) first return map of the Poincaré section of (c). Each point of coordinates  $(I_n, I_{n+1})$  is represented by the number  $p$  of undulations that separate the  $n$ th and the  $(n + 1)$ th crossings through the Poincaré section. The symbols O, I, +, and x correspond, respectively, to  $p = 0, 1, 2$ , and 3. The dashed curves separate regions corresponding to a given  $p$ , which is indicated for each region at the top of each figure. The experimental conditions are given in the text.

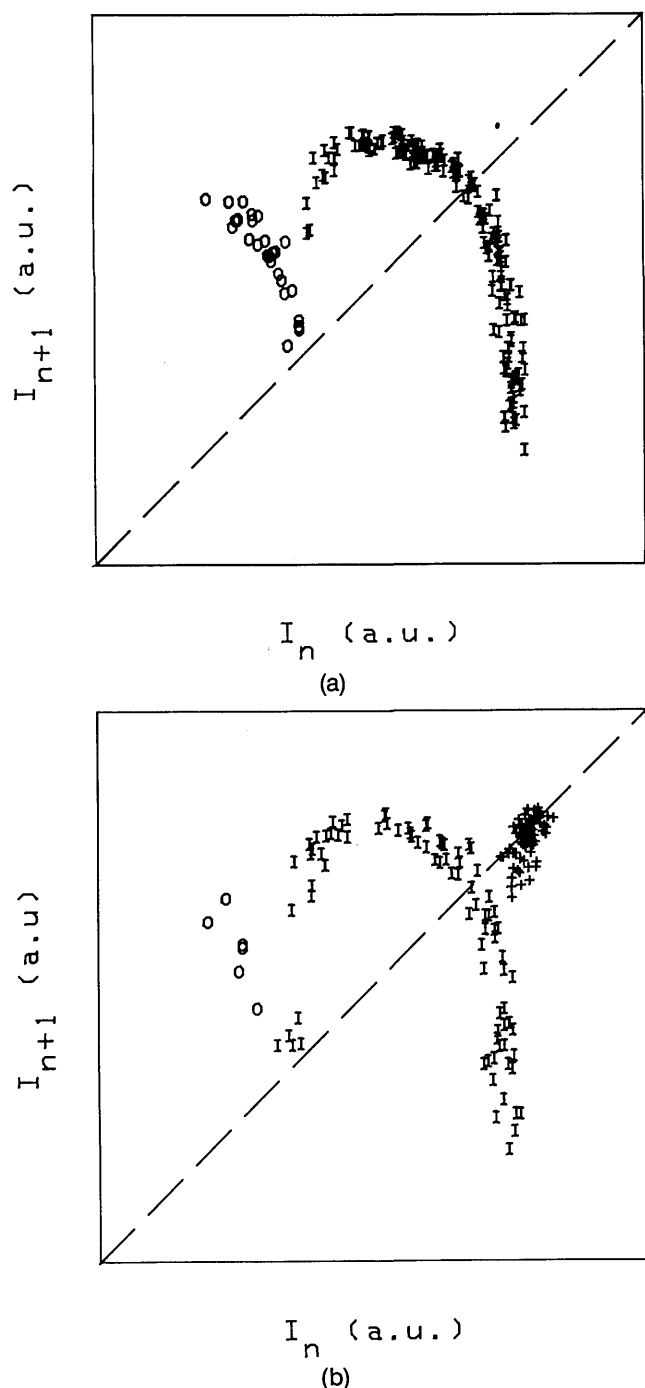


Fig. 2. 1-D maps of  $C^{(1)}$  chaos: (a) close to the  $P^{(1)}$  regime, (b) close to the  $P^{(2)}$  regime. The symbols are the same as in Fig. 1(d).

branches becomes infinite as the system approaches the homoclinic bifurcation.<sup>24,27</sup>

Experimentally, the only accessible variable of the flow is the laser intensity. An example of its temporal evolution in a  $C^{(n)}$  regime is shown in Fig. 1(a) for  $n = 2$ . The signal shows a succession of  $P^{(p)}$ -type pulses with  $p \leq 3$ . The 1-D map is obtained in three steps: (i) A reconstruction of the attractor is undertaken, using the time-delay method. A projection of this attractor in the three-dimensional space  $I(t)$ ,  $I(t + \tau)$ ,  $I(t + 2\tau)$ , with  $\tau = 3.2 \mu\text{sec}$  (i.e.  $\sim T/7$ , where  $T$  is the period of the small

undulations), is shown in Fig. 1(b). It is composed of a spiraling part diverging from  $I_+$  and of a reinjection loop, which, in this three-dimensional representation, passes close to  $I_0$ . (ii) A Poincaré section of this attractor is then obtained at  $I(t)$  constant [Fig. 1(c)]. The value of the constant is chosen so that the Poincaré section plane cuts the trajectory in the middle of the reinjection loop, on the ascending part of the loop [dashed line of Fig. 1(a)]. (iii) Eventually the first return map associated with this section is plotted. As the Poincaré section lies almost on a straight line, this return map is equivalent to a 1-D map. The first return map  $I_n(t + \tau)$ ,  $I_{n+1}(t + \tau)$  obtained for the  $C^{(2)}$  regime is shown in Fig. 1(d). Three branches appear clearly, and the beginning of a fourth one may be seen in the top right-hand corner of the figure. Additional information is provided by counting the number of small undulations separating the two crossings through the Poincaré section associated with each point. The dashed curves in Fig. 1(d) define regions where the same number of undulations are found. It is clear that each region corresponds to a branch. Note that the distance between the branches decreases when  $p$  increases. All these properties hold for other experimentally observed  $C^{(n)}$  regimes. The entire behavior described above is consistent with the properties of homoclinic chaos and supports its existence in the LSA.<sup>24</sup>

The characterization of the behavior can be refined by studying the evolution of the chaos between the  $P^{(n)}$  and  $P^{(n+1)}$  regimes. The passage from  $P^{(n)}$  to  $C^{(n)}$  is well understood, as it occurs through a cascade of period-doubling bifurcations. On the other hand, the passage from  $C^{(n)}$  to  $P^{(n+1)}$  in the LSA has not been discussed. We have plotted the 1-D maps of the  $C^{(1)}$  regime in a region close to  $P^{(1)}$  [Fig. 2(a)] and in a region close to  $P^{(2)}$  [Fig. 2(b)]. In the first case, only the two branches corresponding to  $p = 0$  and  $p = 1$  are visible, whereas in the second case the beginning of a third branch corresponding to  $p = 2$  appears below the 45° line. This may be considered part of the third branch of the  $C^{(2)}$  regime [Fig. 1(d)]. Although the control parameter noise prevents our bringing our system close to the bifurcation, the transition from  $C^{(1)}$  to  $P^{(2)}$  might be interpreted as follows: When the system evolves to  $P^{(2)}$ , a third branch appears in the first return map below the 45° line, approaching it tangentially. Finally,  $P^{(2)}$  appears through a tangent bifurcation. The other experimentally observed  $C^{(n)}$ - $P^{(n+1)}$  transitions evolve in the same way. This behavior, completed by the fact that the transition from the  $P^{(n)}$  to the  $C^{(n)}$  regime occurs through a period-doubling cascade, corresponds exactly to the one exhibited by homoclinic chaos. These results confirm that the  $\text{CO}_2 + \text{CH}_3\text{I}$  LSA in our experimental conditions exhibits a dynamical behavior consistent with the properties known for Shil'nikov chaos.

### 3. MODEL OF THE LASER CONTAINING A SATURABLE ABSORBER

The various theoretical models of the PQS LSA differ in the number of molecular levels considered. Early models aimed at a quantitative agreement for particular experimental parameters and included a large number of variables to model the relaxation processes.<sup>1,2</sup> In an attempt to reach a more global description of the LSA with the

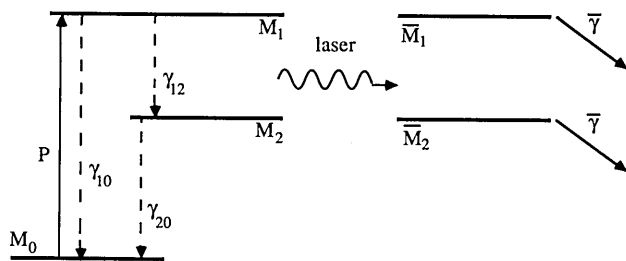


Fig. 3. Schematic representation of the energy levels used in the theoretical model of the LSA. The quantities with overbars refer to the absorber medium, those without overbars to the active medium.

simplest model, Powell *et al.* introduced a two-level description for the absorber and the active medium,<sup>28</sup> which displays a rich phenomenology if molecular polarization and cavity detuning are taken into account.<sup>29</sup> However, this model could hardly provide the range of parameters in which instabilities appear in the CO<sub>2</sub> LSA. For this reason, Arimondo *et al.*<sup>3</sup> proposed including the vibrational manifolds to which the lasing and absorbing levels are coupled, thus reproducing well the experimental domain of existence of PQS.

Nevertheless, there remained a qualitative discrepancy, since this four-level model is unable to predict the  $P^{(n)}$  regimes observed experimentally. A definite step toward such prediction was made by Tachikawa and co-workers,<sup>7,8,10</sup> who introduced the ground state of the CO<sub>2</sub> molecule as a third level for the active medium. With this model other authors were able to obtain the  $P^{(n)}$  periodic states and the  $C^{(n)}$  erratic ones numerically.<sup>14,15</sup> Although Tachikawa's model neglects the influence of inhomogeneous broadening, it provides surprisingly good agreement with experimental observations.

We shall therefore use this model, which is schematically represented in Fig. 3, in numerical simulations to determine whether the different features reminiscent of homoclinic chaos observed experimentally can be reproduced.

The equations, verified by the photon density  $\phi$ , the population densities of the upper lasing level ( $M_1$ ), the lower level ( $M_2$ ), and the ground state ( $M_0$ ) and the population difference in the absorber  $\bar{M}$ , are

$$\dot{\phi} = \phi(\zeta\mathcal{A}(M_1 - M_2) - \bar{\zeta}\bar{\mathcal{A}}\bar{M} - 2\kappa), \quad (1a)$$

$$\dot{M}_1 = -\mathcal{A}(M_1 - M_2)\phi + PM_0 - (\gamma_{10} + \gamma_{12})M_1, \quad (1b)$$

$$\dot{M}_2 = \mathcal{A}(M_1 - M_2)\phi - \gamma_{20}M_2 + \gamma_{12}M_1, \quad (1c)$$

$$\dot{M}_0 = \gamma_{10}M_1 + \gamma_{20}M_2 - PM_0, \quad (1d)$$

$$\dot{\bar{M}} = -2\bar{\mathcal{A}}\phi\bar{M} - \bar{\gamma}(\bar{M} - \bar{M}^*), \quad (1e)$$

where  $\zeta$  ( $\bar{\zeta}$ ) is the relative length of the amplifying (absorbing) medium,  $P$  is the pumping rate,  $2\kappa = cT/L$  is the cavity-damping rate,  $L$  is the total cavity length,  $T$  is the mirror transmittivity,  $\bar{M}^*$  is the equilibrium population in the absorber, and  $\mathcal{A}(M_1 - M_2)$  ( $\bar{\mathcal{A}}\bar{M}$ ) is the saturated amplification (absorption) coefficient.  $\gamma_{ij}$  are the relaxation rates from level  $i$  to level  $j$ , and  $\bar{\gamma}$  is the relaxation rate of the absorber's population inversion. This set of equations is just a generalization of the two-level rate-equation model of the LSA, modified to take into account the pres-

ence of the third level in the active medium and in which only the most relevant relaxation mechanisms have been included. The amplification coefficient  $\mathcal{A}$  is corrected to take into account the rotational partition function and the level degeneracy factor, since emission occurs between two rotational levels not represented in this model. Note also that spontaneous emission has been neglected in the equation for the photon density.

As  $M_0 + M_1 + M_2 = N$  is a constant, a change of variables can then be undertaken to express the dynamics of the LSA in terms of the evolution of the active molecule population difference  $M = M_1 - M_2$  and the dimensionless intensity  $I = 2\mathcal{A}\phi/\gamma_2$ :

$$\dot{I} = I(\zeta\mathcal{A}M - \bar{\zeta}\bar{\mathcal{A}}\bar{M} - 2\kappa), \quad (2a)$$

$$\dot{M} = -(I + 1)\gamma_2 M + PM_0 + \gamma_1(N - M_0), \quad (2b)$$

$$\dot{M}_0 = \gamma_2 N - \gamma_1 M - (\gamma_2 + P)M_0, \quad (2c)$$

$$\dot{\bar{M}} = -2\bar{\mathcal{A}}\phi\bar{M} - \bar{\gamma}(\bar{M} - \bar{M}^*), \quad (2d)$$

where the combined relaxation rates  $\gamma_2 = (\gamma_{20} - \gamma_{10} - 2\gamma_{12})/2$  and  $\gamma_1 = (\gamma_{20} + \gamma_{10} + 2\gamma_{12})/2$  have been introduced as well as the total density of molecules in the amplifier  $N = M_0 + M_1 + M_2$ .

In Eq. (2b) the term  $PM_0 + \gamma_1(N - M_0)$  may be considered a source term. When the relaxation rates are such that  $\gamma_{10} + 2\gamma_{12} = \gamma_{20}$ , the source term is reduced to  $PM_0$ , and the model reduces to a two-level model for both the absorber and the amplifier since Eq. (2c) is no longer coupled to the other ones.

Introducing dimensionless quantities

$$a = \frac{\bar{\mathcal{A}}}{\mathcal{A}} \frac{\gamma_2}{\bar{\gamma}}, \quad b = \left(\frac{\gamma_1}{\gamma_2}\right)^2,$$

$$\varepsilon = \frac{\gamma_2}{2\kappa}, \quad \bar{\varepsilon} = \frac{\bar{\gamma}}{2\kappa},$$

$$A = P(\sqrt{b} + 1) \frac{\mathcal{A}_L N}{2\kappa\gamma_2}, \quad \bar{A} = \bar{M}^* \frac{\bar{\zeta}\bar{\mathcal{A}}}{2\kappa},$$

$$U = M\zeta \frac{\mathcal{A}}{2\kappa}, \quad \bar{U} = \bar{M}\bar{\zeta} \frac{\bar{\mathcal{A}}}{2\kappa},$$

a new variable representing the source term

$$W = \frac{\mathcal{A}}{2\kappa} \frac{\zeta}{\gamma_2} [PM_0 + \gamma_1(N - M_0)],$$

and a dimensionless time  $t' = 2\kappa t$ , we can reformulate Eqs. (2) as follows:

$$\dot{I} = I(U - \bar{U} - 1), \quad (3a)$$

$$\dot{U} = \varepsilon[W - U(1 + I)], \quad (3b)$$

$$\dot{W} = \varepsilon(A + bU - W), \quad (3c)$$

$$\dot{\bar{U}} = \bar{\varepsilon}[\bar{A} - \bar{U}(1 + aI)]. \quad (3d)$$

In Eq. (3c) the  $P/\gamma_2$  term has been considered negligible compared to unity, in good agreement with the values chosen by Tachikawa *et al.*<sup>9</sup> and those used in our numerical estimations ( $P/\gamma_2 < 1.5 \times 10^{-3}$ ).

The threshold of the laser occurs at  $A = A_{th} = (A + 1)(1 - b)$ . Above this threshold, Eqs. (3) have two

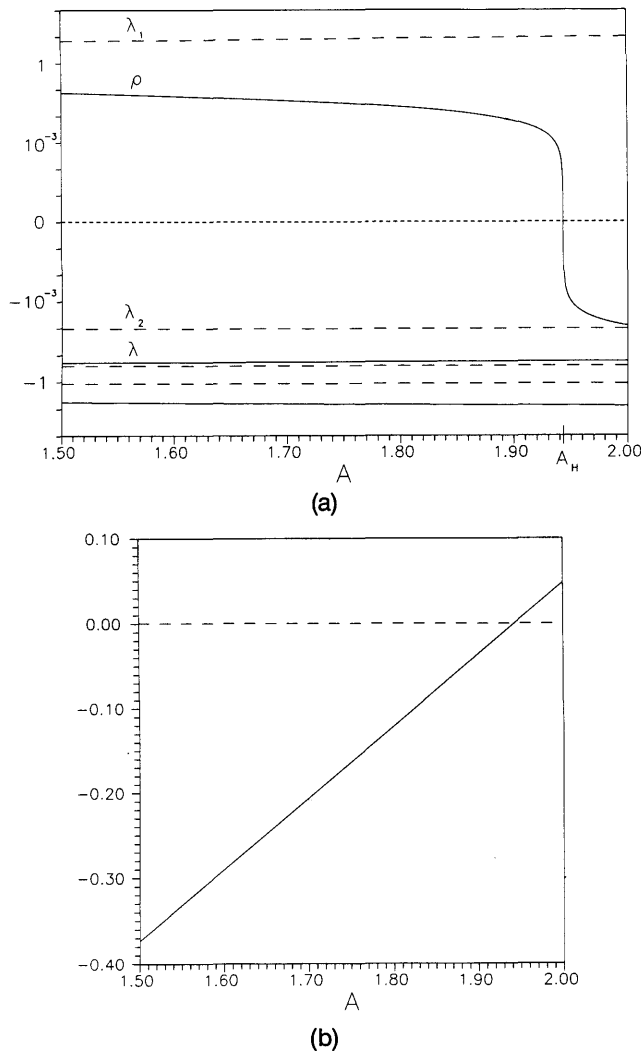


Fig. 4. (a) Evolution of the eigenvalues of the  $I_0$  (dashed lines) and the  $I_+$  (solid lines) eigenvalues as functions of the  $A$  parameter.  $A_H = 1.943$  is the Hopf bifurcation point. (b) Values of  $\rho/\lambda$  (solid line) and  $(\lambda_2/\lambda_1)(\rho/\lambda)$  (dashed line) versus  $A$ . Their absolute values are both smaller than 1.

stationary solutions corresponding in phase space to two fixed points  $I_0$  and  $I_+$  whose coordinates  $(I_0, U_0, W_0, \bar{U}_0)$  and  $(I_+, U_+, W_+, \bar{U}_+)$  are

$$I_0 = 0, \quad U_0 = W_0 = A(1 - b)^{-1}, \quad \bar{U}_0 = \bar{A},$$

$$I_+ = \frac{\alpha(A + b - 1) - (\bar{A} + 1) + \{[a(A + b - 1) - (\bar{A} + 1)]^2 + 4a(A - A_{th})\}^{1/2}}{2a},$$

$$U_+ = A(1 + I_+ - b)^{-1},$$

$$W_+ = A(1 + I_+)(1 + I_+ - b)^{-1},$$

$$\bar{U}_+ = \bar{A}(1 + aI_+)^{-1}.$$

A linear stability analysis provides the eigenvalues of the linear flow in the vicinity of these two fixed points. With parameters corresponding to our experiments, the stability of  $I_0$  is characterized by four real eigenvalues ( $\lambda_1, \lambda_2, \lambda_3$ , and  $\lambda_4$ , where  $\lambda_1$  is positive and corresponds to an eigenvector collinear to the intensity vector and  $\lambda_2, \lambda_3$ , and  $\lambda_4$  are negative,  $|\lambda_4| \geq |\lambda_3| \geq |\lambda_2|$ ), and  $I_+$  is associated with two real negative eigenvalues ( $\lambda$  and  $\lambda'$ ,  $|\lambda'| \geq |\lambda|$ ) and

two complex-conjugate eigenvalues ( $\rho \pm i\omega$ , where  $\rho$  is positive).  $I_0$  is therefore a saddle point whose unstable manifold is along the intensity direction and  $I_+$  is a saddle focus. These eigenvalues are plotted versus the pump parameter in Fig. 4. Note that the eigenvalues of  $I_+$  have real parts with different orders of magnitude: for typical values of the parameters,  $|\lambda'| \approx 30|\lambda| \approx 300|\rho|$ . Therefore one expects that, near  $I_+$ , the eigendirection corresponding to  $\lambda'$  will be irrelevant and that  $I_+$  will be equivalent to a three-dimensional saddle-focus fixed point with eigenvalues  $\lambda, \rho \pm i\omega$ . Note that the eigenvector corresponding to  $\lambda'$  is quasi-orthogonal to the  $(U, W)$  plane, indicating that these two variables, which describe the amplifying medium, evolve on a slow time scale.

The dynamics of the system depends strongly on the relative values of the eigenvalues of  $I_+$  and of the global structure of the flow. Shil'nikov showed that if a homoclinic orbit is associated with a saddle focus such as  $I_+$ , and if in the neighborhood of this point the characteristic time of the flow following the focus directions is the largest one ( $\rho/\lambda < 1$ ), the system has a chaotic behavior.<sup>19</sup> This is a sufficient condition but not a necessary one. In particular, if the unstable and the stable manifolds are not perfectly connected but close to form a homoclinic orbit, chaos may occur.<sup>30</sup> The values of  $\rho/\lambda$  are plotted in Fig. 4(b) for the set of parameters discussed in Section 4. It is clear that the Shil'nikov condition for chaos is fulfilled, but, as the existence of a homoclinic orbit cannot be predicted analytically, only a numerical resolution of the equations will allow the presence of chaos to be inferred.

The situation is complicated here by the presence of the second fixed point,  $I_0$ . Either of two limit configurations is possible: (i) The two points are coupled by a homoclinic cycle, which connects the unstable manifold of  $I_+$  to the stable manifold of  $I_0$  and the unstable manifold of  $I_0$  to the stable manifold of  $I_+$ . In this case, the Shil'nikov condition for chaos becomes  $|(\lambda_2/\lambda_1)(\rho/\lambda)| < 1$ ,<sup>39</sup> indicating that too large an attractive power of  $I_0$  ( $\lambda_2$  large) will destroy the chaos by rescaling the trajectory at each passage in the vicinity of  $I_0$ . (ii) The two points are completely decoupled, and their respective stable and unstable manifolds always remain far from the conditions of intersection. In this case, a trajectory coming from  $I_+$  always remains out of reach from  $I_0$ , which does not interfere in the dynamics. Between these two limit cases a large number of possible intermediate configurations exists in

which the influence of  $I_0$  evolves with the strength of the coupling between the two fixed points.

Figure 4(b) shows the values of  $(\lambda_2/\lambda_1)(\rho/\lambda)$  for the same set of parameters as above. It appears that the product  $|(\lambda_2/\lambda_1)(\rho/\lambda)|$  is negligible compared to 1, so that, if we are in the case of strong coupling between the two fixed points, the effect of the  $I_0$  point will be to increase the sensitivity to initial conditions of the trajectories emerging from  $I_+$ . Consequently we can conclude that, provided that the system is close to a homoclinic or heteroclinic bifurcation, chaotic behavior will be observed, since sufficient conditions for the presence of homoclinic chaos hold true in both cases.

**Table 1. Values of the Parameters Used in the Numerical Simulations**

Parameter	Value
$A$	1.4 to 2.1
$\gamma_{20}$	$2.892 \times 10^5 \text{ sec}^{-1}$
$\gamma_{10}$	$1.2 \times 10^6 \text{ sec}^{-1}$
$\gamma_{12}$	$10 \text{ sec}^{-1}$
$\bar{A}$	2.16
$\bar{\gamma}$	$1.3 \times 10^6 \text{ sec}^{-1}$
$\varepsilon$	0.137
$\bar{\varepsilon}$	1.2
$b$	0.85
$a$	4.17
$2\kappa$	$1.1 \times 10^6 \text{ sec}^{-1}$

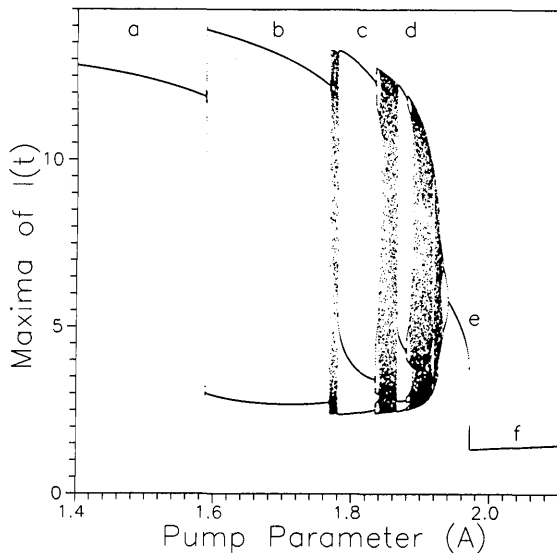


Fig. 5. Bifurcation diagram of the model of the LSA for parameters of Table 1. The letters indicate the following regimes: a,  $P^{(0)}$ ; b,  $P^{(1)}$ ; c,  $P^{(2)}$ ; d,  $P^{(3)}$ ; e,  $T$ ; f,  $I_+$ .

#### 4. NUMERICAL RESULTS

In our experiments the main control parameter is the frequency detuning. As we assume that its main effect is to change the pump parameter  $A$ ,<sup>11</sup> this quantity has been chosen as a control parameter in the following numerical study, and all other parameters are fixed to the values given in Table 1.

In Fig. 5 we show a bifurcation diagram corresponding to the values of Table 1 in which the pump parameter  $A$  is varied from 1.4 to 2.1. For each parameter value successive maxima of the  $I$  variable are plotted. This allows us to characterize the chaotic regimes, the  $P^{(n)}$  ones, and their period doublings.

The calculated bifurcation diagram is close to the experimental behavior: the  $P^{(n)}$  states with  $n \leq 3$  are present and are separated by chaotic regimes  $C^{(n)}$ , except that  $P^{(0)}$  and  $P^{(1)}$  experience bistability, as is often seen experimentally. The transition from  $P^{(n)}$  to  $C^{(n)}$  occurs through a cascade of period-doubling bifurcations.  $C^{(n)}$  signals are characterized by a quasi-random sequence of  $P^{(m)}$ -like pulses, with  $0 \leq m \leq n$  or  $0 \leq m \leq n + 1$ , depending on whether we are closer in parameter space to the  $P^{(n)}$  or to the  $P^{(n+1)}$  periodic window. The  $T$  regime

(type II PQS), which appears after a subcritical Hopf bifurcation, and the successive period-doubled orbits can also be seen on the right-hand side of the Fig. 5. We shall see in the what follows that the subcritical nature of the Hopf bifurcation is a crucial point. The experimental transition from steady state to PQS appears to be subcritical or supercritical, depending on the operating conditions (e.g., see Refs. 3, 5, and 10), and it would be of interest to determine the boundary between the two kinds of behavior since supercritical bifurcations are observed numerically for smaller  $\bar{\varepsilon}$ .

Figures 6(a) and 7(a) show examples of the time evolution of the laser intensity inside the  $C^{(1)}$  and the  $C^{(2)}$  chaotic regions, respectively, of the bifurcation diagram that are quite similar to experimental signals. To compute the 1-D return maps associated with these regimes and compare them with experimental results, a Poincaré section plane must be fixed. To get the multibranch maps characteristic of the homoclinic chaos, we choose a plane of constant intensity, which is crossed once and only once between two reinjection loops corresponding to the large peaks in the temporal signal.

The Poincaré sections for  $A = 1.773$  and  $A = 1.86$  are shown in Figs. 6(b) and 7(b), respectively. Whereas the model is four dimensional, strong volume contraction occurs, and the projections of the sections on the  $(U, W)$  plane are seen to be quasi-1-D. Indeed, on computing the Lyapunov exponents for, e.g.,  $A = 1.86$ , one finds the values 0.0168, 0.0,  $-0.191$ , and  $-7.81$  inverse reduced time units, yielding from the Kaplan-Yorke formula<sup>31</sup> a Lyapunov dimension of 2.088, which is known to be an upper bound on the fractal dimension.<sup>32</sup> A projection of the corresponding attractor in the  $(I, U, W)$  subspace is displayed in Fig. 7(d). The fractal dimension is therefore close to 2, suggesting that a phenomenological model involving only three variables could in principle be found. This fact allows us to construct 1-D return maps  $U_{n+1} = f(U_n)$ , which are shown in Figs. 6(c) and 7(c). They are seen to have exactly the same structure as those observed experimentally, although they are computed in the  $(I, U, W, \bar{U})$  phase space instead of in a reconstructed attractor.

Similar 1-D maps can be plotted for the other chaotic regimes and display the same features. In a general way, the first return map of a  $C^{(n)}$  regime shows  $n + 1$  or  $n + 2$  branches corresponding to the  $P^{(m)}$  pulses of the temporal signal. The appearance of the  $(n + 2)$ th branch in the  $C^{(n)}$  region is linked with the proximity of the tangent bifurcation in which the  $P^{(n+1)}$  periodic orbit is created. Indeed, as the  $P^{(n)}$  window is approached, the  $(n + 2)$ th branch comes closer and closer to the  $U_{n+1} = U_n$  line and eventually becomes tangent to it. Beyond the bifurcation, a stable and an unstable fixed point appear, the stable one corresponding to the  $P^{(n+1)}$  state. To confirm this observation, we have computed the transverse Floquet multipliers of the  $P^{(3)}$  regime inside its domain of stability. Two are always small, owing to strong dissipation, and the evolution of the other has been plotted in Fig. 8. The value  $-1$  for  $A = 1.8780$  corresponds to the period-doubling bifurcation of  $P^{(3)}$ , and the value 1 for  $A = 1.8647$  clearly shows that the transition from  $C^{(2)}$  to  $P^{(3)}$  occurs through a tangent bifurcation. This has also been verified for other bifurcations from  $C^{(n)}$  to  $P^{(n+1)}$ . In the vicinity of the

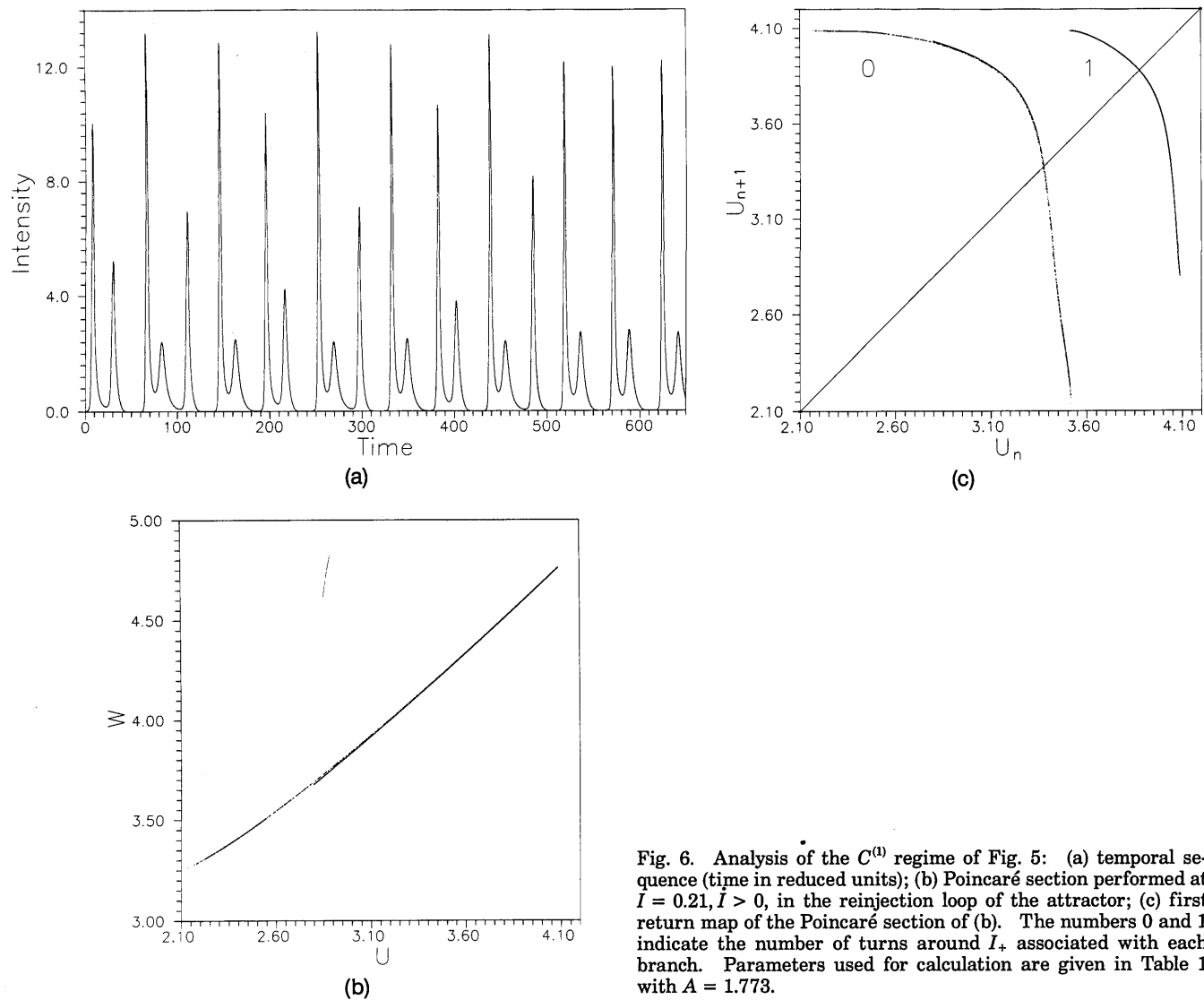


Fig. 6. Analysis of the  $C^{(1)}$  regime of Fig. 5: (a) temporal sequence (time in reduced units); (b) Poincaré section performed at  $\bar{I} = 0.21, \bar{I} > 0$ , in the reinjection loop of the attractor; (c) first return map of the Poincaré section of (b). The numbers 0 and 1 indicate the number of turns around  $I_+$  associated with each branch. Parameters used for calculation are given in Table 1 with  $A = 1.773$ .

transition, there is type I intermittency, whose reinjection mechanism is deeply connected with the Shil'nikov dynamics. Recall that the creation of periodic orbits with increasing numbers of undulations by tangent bifurcations is one of the main characteristics of homoclinic chaos.<sup>18,33</sup>

Whereas both the scenario observed when  $A$  is varied and the 1-D maps shown strongly favor the hypothesis of homoclinic chaos in the model studied, no homoclinic bifurcation can be located for the parameters used so far. This means that our one-parameter path does not intersect the codimension-1 subset of parameter space where homoclinic bifurcations take place. We have therefore varied another parameter,  $\bar{\varepsilon}$ , which controls the time scale on which the absorber evolves. We stress that this does not mimic experimental operation, as increasing the absorber pressure, for example, would result in a higher  $\bar{\varepsilon}$  but would also decrease the relative saturability  $\alpha$ . Nevertheless, it corresponds to using a much more saturable absorber (for instance,  $SF_6$ ) with a buffer gas. Looking at the different bifurcation diagrams obtained for increasing  $\bar{\varepsilon}$ , we find that the various  $P^{(n)}$  regimes with increasing numbers of undulations appear successively in the bifurcation diagram in a continuous way, without changing its

global structure, as can be seen from Fig. 9, indicating that we come closer to homoclinicity.

Since the numerical integration time increases rapidly with  $\bar{\varepsilon}$ , it was not possible to determine the value of  $\bar{\varepsilon}$  above which a homoclinic bifurcation is encountered in the bifurcation diagram with control parameter  $A$ . Nevertheless, in the limit case  $\bar{\varepsilon} \rightarrow \infty$ , where the absorber's population inversion can be adiabatically eliminated, leading to a three-variable model, we find an homocliniclike bifurcation, in the neighborhood of which chaotic regimes with as many as 41 undulations, as in Fig. 10 for  $A = 1.997$ , could be located. Hence it is highly likely that the global structure of the bifurcation diagram obtained with parameters of Table 1 can be traced back to the existence of such bifurcations for higher values of  $\bar{\varepsilon}$ . We shall therefore concentrate in what follows on the model obtained for infinite  $\bar{\varepsilon}$  and study the nature of the observed bifurcation. Figure 11 shows the corresponding bifurcation diagram.

We stress that the  $P^{(n)}$  and  $C^{(n)}$  solutions of this model for the lowest  $n$  are similar to those obtained in the model with four variables, as can be seen from Fig. 12 for the  $C^{(2)}$  regime. The fact that the same type of dynamics is

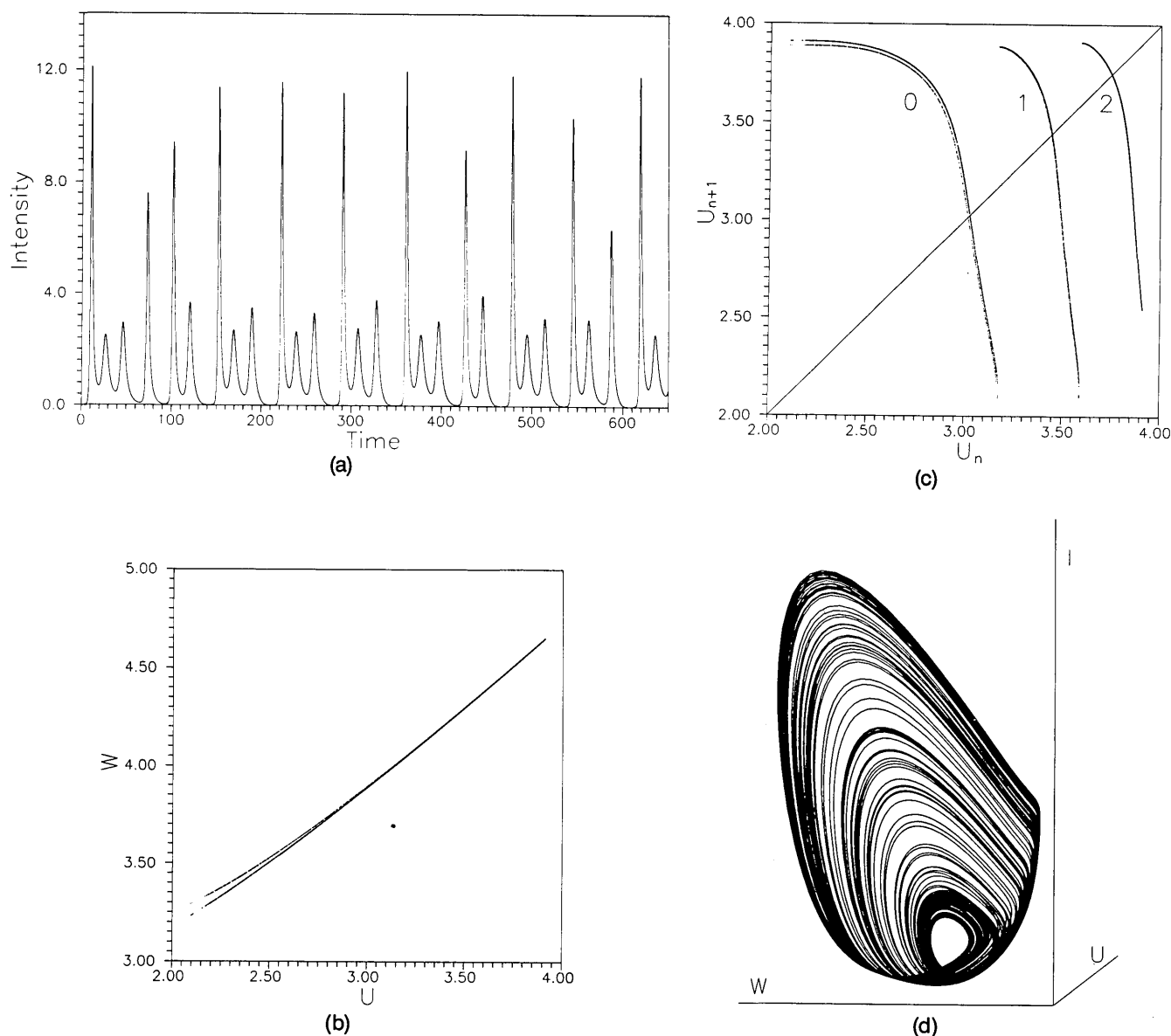


Fig. 7. Analysis of the  $C^{(2)}$  of the diagram of Fig. 5: (a) Temporal sequence (time in reduced units). (b) Poincaré section performed at  $I = 0.21$ ,  $I > 0$ , in the reinjection loop of the attractor. (c) First return map of the Poincaré section of (b). 0–2 indicate the number of turns associated with each branch. (d) Projection of the attractor on the hyperplane  $(I, U, W)$ . The parameters used for calculation are given in Table 1 with  $A = 1.860$ .

found indicates that the characteristic time scale of the absorber is not a crucial parameter when one is looking from homocliniclike behavior. In fact, as was already suggested,<sup>9</sup> the origin of the PQS behavior is the slow relaxation rate from the low level of the laser transition to the ground level.

Some facts about the behavior observed for infinite  $\bar{\epsilon}$ , however, contrast with the standard Shil'nikov configuration involving a saddle-focus fixed point:

(i) The  $I_+$  fixed point is stable at the parameter value at which the bifurcation occurs.

(ii) The amplitude of the undulations never shrinks to zero and is always greater than a minimum value.

(iii) All the  $P^{(n)}$  and  $C^{(n)}$  states are found on one side only of the bifurcation instead of lying symmetrically on each side.

These three facts lead to believe that we in fact observe in the reduced model a homoclinic tangency to an unstable periodic orbit with positive Floquet multipliers.<sup>33</sup> Using a standard method to find periodic orbits and follow them for changing parameters,<sup>34</sup> we were able to locate precisely the unstable cycle around which the flow spirals and determine its transverse Floquet multipliers near homoclinicity,  $\lambda_u = 1.1326$  and  $\lambda_s = 0.05646$ . We also discovered that this cycle corresponds to the unstable cycle created at the subcritical Hopf bifurcation of  $I_+$  for  $A \approx 1.974$  and annihilated for higher  $A$  in a saddle-node bifurcation with the  $T$  periodic orbit for  $A \approx 2.034$ . As it corresponds to an infinite number of undulations, hereafter it will be called  $P^{(\infty)}$ .

For evidence that a homoclinic tangency to  $P^{(\infty)}$  occurs in the model for  $A \approx 1.997$ , we computed the stable and unstable manifolds  $W_s$  and  $W_u$ , respectively, of  $P^{(\infty)}$  for

parameter values  $A = 1.997$  and  $A = 1.991$ . The intersection of these manifolds with a section plane transverse to  $P^{(\infty)}$  is shown in Fig. 13. It is clear that, for  $A = 1.997$ ,  $W_u$  and  $W_s$  become tangent so that a homoclinic orbit that is biasymptotic to the unstable cycle is created.<sup>33</sup> For  $A < 1.997$  the stable manifold acts as a separatrix and prevents the trajectories that spiral around  $P^{(\infty)}$  from reaching  $I_+$ . This explains the generalized bistability observed between  $I_+$  and the  $P^{(n)}$  and  $C^{(n)}$  regimes for  $n > 8$  ( $1.974 < A < 1.997$ ). For  $A > 1.997$ ,  $W_u$  intersects  $W_s$  transversally, so that the attraction basin of  $I_+$  extends beyond  $P^{(\infty)}$ . This is why a sudden transition from chaos to a constant-intensity region is observed in the bifurcation diagram of Fig. 11 when  $A = 1.997$  is reached. There is still bistability between the period-doubling cascade of the  $T$  regime and  $I_+$  for  $1.997 < A < 2.034$ , but  $P^{(\infty)}$  is no longer involved.

It is interesting to note that the 1-D maps computed in the case of a homoclinic tangency to a cycle, as in

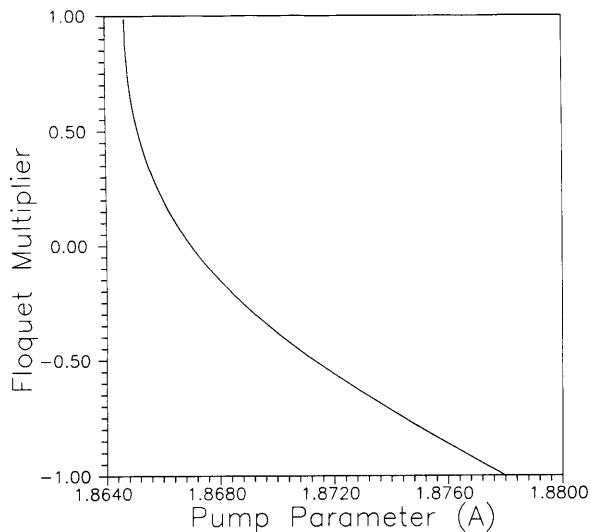
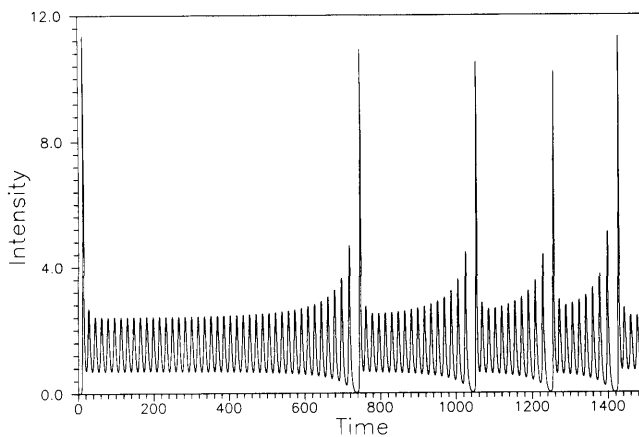
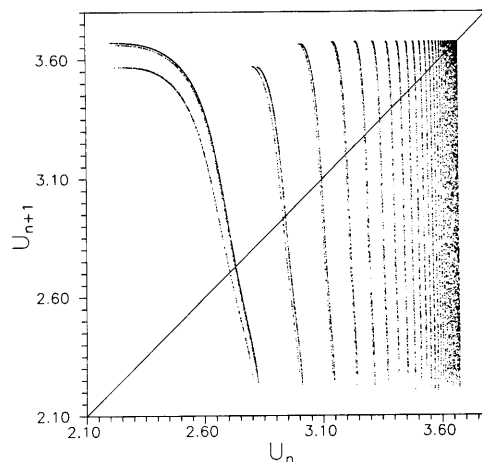


Fig. 8. Plot of the largest transverse Floquet multiplier associated with the  $P^{(3)}$  periodic orbit as a function of  $A$ .



(a)



(b)

Fig. 10. (a) Temporal signal obtained for  $A = 1.997$  with the reduced model ( $\bar{\epsilon}$  infinite). A pulse with 41 undulations can be seen. (b) First return map of the Poincaré section plane  $I = 0.2, I > 0$ , with 42 branches. The branches converge geometrically with an asymptotic rate equal to 0.882. Except for  $\bar{\epsilon}$ , the parameters may be found in Table 1, as they can for Figs. 11-13.

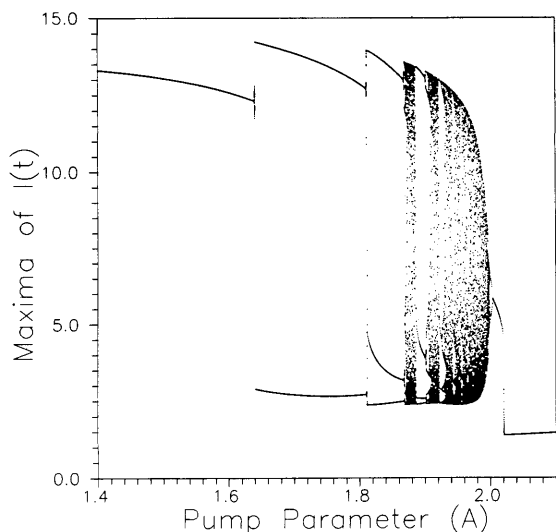


Fig. 9. Bifurcation diagram of the model of the LSA for the parameters of Table 1, except for  $\bar{\epsilon} = 6$ . Periodic regimes  $P^{(n)}$  with  $n \leq 8$  are present.

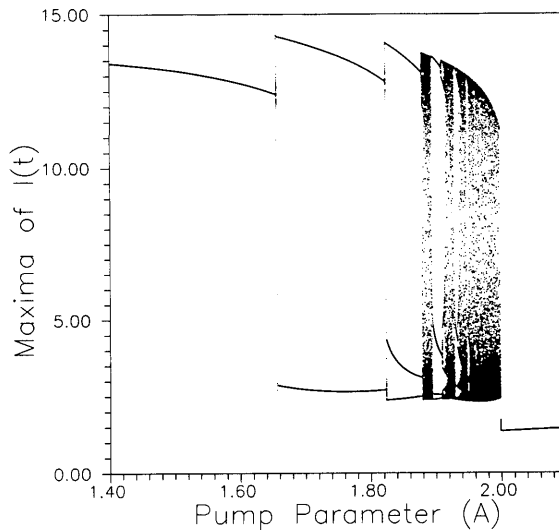


Fig. 11. Bifurcation diagram obtained with infinite  $\bar{\epsilon}$ . The sudden transition from chaos to  $I_+$ , which can be seen at the right, corresponds to a homocliniclike bifurcation.

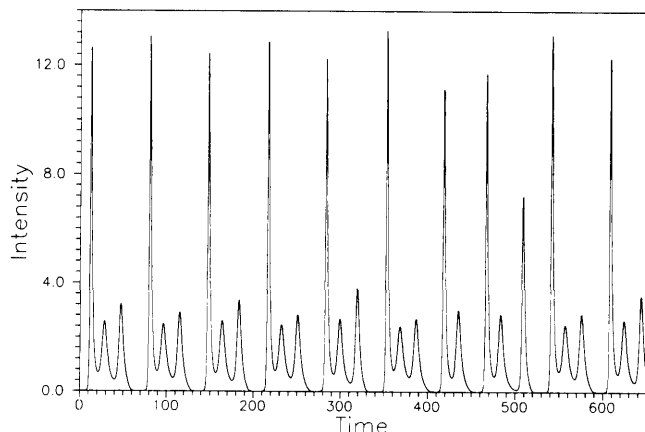


Fig. 12. Temporal signal obtained for  $A = 1.888$  with the reduced model ( $\bar{\epsilon}$  infinite). It is similar to signals of the four-variable model computed for equivalent pump parameters and may be compared with Fig. 7(a).

Fig. 10, have exactly the properties that were originally established<sup>24,27</sup> in the case of a saddle-focus fixed point. We cannot therefore exclude the possibility that the 1-D maps observed experimentally are related to a homoclinic tangency.

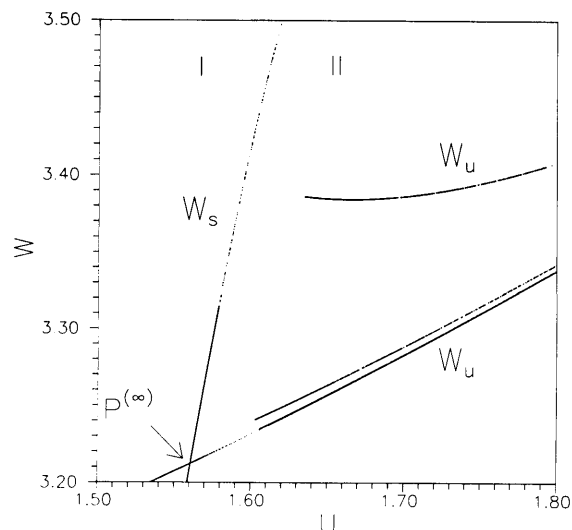
The fact that the unstable cycle  $P^{(\infty)}$  involved in the homoclinic tangency is created in the Hopf bifurcation of  $I_+$  is quite important for two reasons:

(i) The  $P^{(n)}$  regimes for  $n \leq 8$  are created, whereas  $P^{(\infty)}$  does not yet exist. This means that this part of the bifurcation diagram is controlled by the saddle focus  $I_+$  as if we were in a standard Shil'nikov situation. As the Hopf bifurcation is encountered, there is a crossover from  $I_+$  to  $P^{(\infty)}$  as the organizing center of the dynamics, since  $I_+$  is then isolated from the remainder of the phase space.

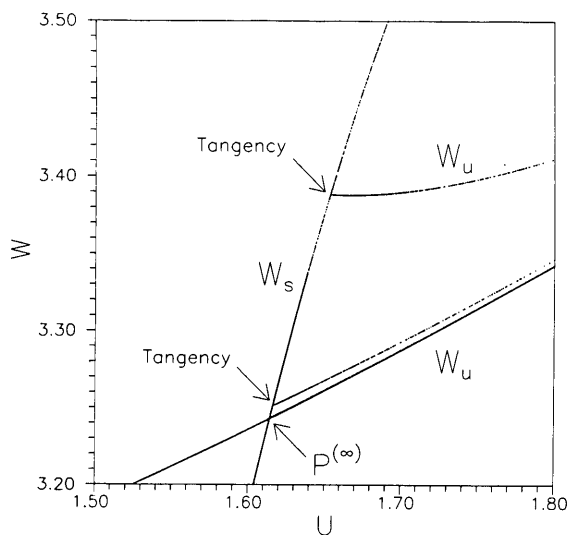
(ii) In experiments with  $\text{CH}_3\text{I}$ , and in numerical simulations as well, a reduction of the amplitude of the undulations of the  $P^{(n)}$  regimes has not been observed; furthermore, no scenario for the type  $\dots C^{(n-1)}, P^{(n)}, C^{(n)}, P^{(n+1)}, \dots, P^{(n+1)}, C^{(n)}, P^{(n)}, C^{(n-1)} \dots$  has been encountered. This suggests that, in the experimental situation, the mechanism leading to chaos involves homoclinicity to a periodic orbit, in the same way as in the numerical study. As the scenario described in the case of a fast absorber can occur only if the Hopf bifurcation is subcritical, working in parameter space regions where  $I_+$  and the PQS regime experience bistability could help in locating a homoclinic tangency experimentally.

## 5. CONCLUSION

Experimental chaotic regimes of the LSA of the type  $C^{(n)}$  have been shown to display the characteristic features of homoclinic chaos through the analysis of first return maps of the signal and the study of the transitions between chaotic and periodic regimes. A now-standard model of the Q-switching LSA has been explored numerically, reproducing the experimental behavior well. The results obtained with a fast absorber suggest that the phase diagram of a LSA is determined largely by a homoclinic tangency to an unstable cycle created in a subcritical Hopf bifurcation, which explains the homocliniclike behavior observed.



(a)



(b)

Fig. 13. Intersection with a section plane transverse to  $P^{(\infty)}$  of the stable ( $W_s$ ) and unstable ( $W_u$ ) manifolds of  $P^{(\infty)}$  in the neighborhood of the unstable cycle. The point where the two manifolds cross is the intersection of  $P^{(\infty)}$  with the section plane: (a) For  $A = 1.991$ ,  $W_s$  and  $W_u$  are disconnected. Region I is the attraction basin of  $I_+$ , and region II is the part of phase space where motion on the attractor takes place. The two regions are separated by  $W_s$ . (b) For  $A = 1.997$ ,  $W_u$  and  $W_s$  are tangent to each other.

## ACKNOWLEDGMENTS

We thank A. Bekkali for his help in the early stages of this study. We are also grateful to A. Arneodo, C. Baesens, P. Coulet, and C. Tresser for fruitful discussions of the properties of Shil'nikov chaos and to E. Arimondo and B. Zambon for stimulating exchanges and for communication to us of their papers and works before publication. We are particularly indebted to P. Glorieux for his advice and numerous suggestions.

## REFERENCES

1. I. Burak, P. L. Houston, D. G. Sutton, and J. I. Steinfeld, "Mechanism of passive Q-switching in  $\text{CO}_2$  lasers," *IEEE J. Quantum Electron.* **QE-7**, 73-82 (1971).

2. J. Dupré, F. Meyer, and C. Meyer, "Influence des phénomènes de relaxation sur la forme des impulsions fournies par un laser CO<sub>2</sub> déclenché par un absorbant saturable," *Rev. Phys. Appl.* **10**, 285–293 (1975).
3. E. Arimondo, F. Casagrande, L. Lugiato, and P. Glorieux, "Repetitive passive Q-switching and bistability in lasers with saturable absorber," *Appl. Phys. B* **30**, 57–77 (1983).
4. M. L. Asquini and F. Casagrande, "Passive Q-switching in lasers with saturable absorbers: improved treatment of a four level method," *Nuovo Cimento* **2D**, 917–931 (1983).
5. A. Jacques and P. Glorieux, "Observation of bistability in a CO<sub>2</sub> laser exhibiting passive Q-switching," *Opt. Commun.* **40**, 455–460 (1982).
6. E. Arimondo and E. Menchi, "Analysis of Q-switch in a CO<sub>2</sub> laser with saturable absorber," *Appl. Phys. B* **37**, 55–61 (1985).
7. M. Tachikawa, K. Tanii, M. Kajita, and T. Shimizu, "Undamped undulation superposed on the passive Q-switching pulse of a CO<sub>2</sub> laser," *Appl. Phys. B* **39**, 83–90 (1986).
8. K. Tanii, M. Tachikawa, M. Kajita, and T. Shimizu, "Sinusoidal self-modulation in the output of a CO<sub>2</sub> laser with an intracavity saturable absorber," *J. Opt. Soc. Am. B* **5**, 24–28 (1988).
9. E. Arimondo, P. Bootz, P. Glorieux, and E. Menchi, "Pulse shape and phase diagram in the passive Q-switching of CO<sub>2</sub> lasers," *J. Opt. Soc. Am. B* **2**, 193–201 (1985).
10. M. Tachikawa, K. Tanii, and T. Shimizu, "Comprehensive interpretation of passive Q-switching and optical bistability in a CO<sub>2</sub> laser with an intracavity saturable absorber," *J. Opt. Soc. Am. B* **4**, 387–395 (1987).
11. B. Zambon, F. de Tomasi, D. Hennequin, and E. Arimondo, "Investigations of models for the laser with a saturable absorber: theoretical and experimental studies of the stationary regimes," *Phys. Rev. A* **40**, 3782–3795 (1989).
12. D. Dangoisse, A. Bekkali, F. Papoff, and P. Glorieux, "Shil'nikov dynamics in a passive Q-switching laser," *Europhys. Lett.* **6**, 335–340 (1988).
13. D. Hennequin, F. de Tomasi, B. Zambon, and E. Arimondo, "Homoclinic orbits and cycles in the instabilities of a laser with saturable absorber," *Phys. Rev. A* **37**, 2243–2246 (1988).
14. M. Tachikawa, K. Tanii, and T. Shimizu, "Laser instability and chaotic pulsation in a CO<sub>2</sub> laser with intracavity saturable absorber," *J. Opt. Soc. Am. B* **5**, 1077–1081 (1988).
15. F. de Tomasi, D. Hennequin, B. Zambon, and E. Arimondo, "Instabilities and chaos in an infrared laser with saturable absorber: experiments and vibrational model," *J. Opt. Soc. Am. B* **6**, 45–57 (1989).
16. M. Tachikawa, F. L. Hong, K. Tanii, and T. Shimizu, "Deterministic chaos in passive Q-switching pulsation of a CO<sub>2</sub> laser with saturable absorber," *Phys. Rev. Lett.* **60**, 2266–2268 (1988).
17. P. Glendinning and C. Sparrow, "Local and global behavior near homoclinic orbits," *J. Stat. Phys.* **35**, 645–696 (1984).
18. P. Gaspard, R. Kapral, and G. Nicolis, "Bifurcation phenomena near homoclinic systems: a two-parameter analysis," *J. Stat. Phys.* **35**, 697–727 (1984).
19. L. P. Shil'nikov, "A case of the existence of a countable number of periodic motions," *Sov. Math. Dokl.* **6**, 163–166 (1965); "A contribution to the problem of the structure of an extended neighborhood of a rough equilibrium state of saddle focus type," *Math. USSR Sbornik* **10**, 91–102 (1970).
20. D. Hennequin, F. de Tomasi, L. Fronzoni, B. Zambon, and E. Arimondo, "Influence of noise on the quasi-homoclinic behavior of a laser with saturable absorber," *Opt. Commun.* **70**, 253–258 (1989).
21. D. Hennequin, M. Lefranc, A. Bekkali, D. Dangoisse, and P. Glorieux, "Characterization of Shil'nikov chaos in a CO<sub>2</sub> laser containing a saturable absorber" in *Measures of Complexity and Chaos*, N. B. Abraham, A. M. Albano, A. Passamente, and P. E. Rapp, eds. (Plenum, New York, 1989), pp. 299–302.
22. F. Papoff, A. Fioretti, E. Arimondo, and N. B. Abraham, "Time return maps and distributions for the laser with a saturable absorber," in *Measures of Complexity and Chaos*, N. B. Abraham, A. M. Albano, A. Passamente, and P. E. Rapp, eds. (Plenum, New York, 1989), pp. 309–312.
23. F. T. Arecchi, A. Lapucci, R. Meucci, J. A. Roversi, and P. H. Coulet, "Experimental characterization of Shil'nikov chaos by statistics of return times," *Europhys. Lett.* **6**, 677–682 (1988); F. T. Arecchi, W. Gadoski, A. Lapucci, H. Mancini, R. Meucci, and J. A. Roversi, "Laser with feedback: an optical implementation of competing instabilities, Shil'nikov chaos, and transient fluctuation enhancement," *J. Opt. Soc. Am. B* **5**, 1153–1159 (1988).
24. F. Argoul, A. Arneodo, and P. Richetti, "Experimental evidence for homoclinic chaos in the Belousov-Zhabotinskii reaction," *Phys. Lett. A* **120**, 269–275 (1987); F. Argoul, A. Arneodo, and P. Richetti, "Dynamique symbolique dans la réaction de Belousov-Zhabotinskii: une illustration expérimentale de la théorie de Shil'nikov des orbites homoclines," *J. Chim. Phys.* **84**, 1367–1385 (1987).
25. E. Arimondo and P. Glorieux, "Saturated absorption experiments on a dressed molecule. Application to the spectroscopy of the  $\nu_6$  band of CH<sub>3</sub>I," *Phys. Rev. A* **19**, 1067–1083 (1979).
26. See, e.g., J. S. Turner, J. C. Roux, W. D. McCormick, and H. L. Swinney, "Alternating periodic and chaotic regimes in a chemical reaction—experiments and theory," *Phys. Lett.* **85A**, 9–12 (1981).
27. A. Arneodo, P. Coulet, E. A. Spiegel, and C. Tresser, "Asymptotic chaos," *Physica D* **14**, 327–347 (1985).
28. H. T. Powell and G. J. Wolga, "Repetitive passive Q-switching of single-frequency lasers," *IEEE J. Quantum Electron.* **QE-7**, 213–219 (1971).
29. T. Erneux and P. Mandel, "Bifurcation phenomena in a laser with saturable absorber I and II," *Z. Phys. B* **44**, 353–363, 365–374 (1981); P. Mandel and T. Erneux, "Stationary, harmonic and pulsed operations of an optically bistable laser with saturable absorber. I and II," *Phys. Rev. A* **30**, 1893–1901, 1902–1909 (1984); T. Erneux, P. Mandel, and J. Magan, "Quasi-periodicity in lasers with saturable absorbers," *Phys. Rev. A* **29**, 2690–2699 (1984); D. E. Chyba, N. B. Abraham, and A. M. Albano, "Semiclassical analysis of a detuned ring laser with a saturable absorber. New results for the steady states," *Phys. Rev. A* **35**, 2936–2950 (1987).
30. C. Tresser, "About some theorems by L. P. Shil'nikov," *Ann. Inst. Henri Poincaré* **40**, 441–461 (1984).
31. P. Fredrickson, J. L. Kaplan, E. D. Yorke, and J. A. Yorke, "The Lyapunov dimension of strange attractors," *J. Diff. Eqs.* **49**, 185–207 (1983).
32. F. Ledrappier, "Some relations between dimension and Lyapunov exponent," *Commun. Math. Phys.* **81**, 229–238 (1981).
33. P. Gaspard and X. J. Wang, "Homoclinic orbits and mixed-mode oscillations in far from equilibrium systems," *J. Stat. Phys.* **48**, 151–199 (1987).
34. C. Sparrow, *The Lorenz Equations, Bifurcations, Chaos and Strange Attractors* (Springer-Verlag, Berlin, 1982), pp. 211–220, App. E.